All-Optical Nonzero-Field Vector Magnetic Sensor for Magnetoencephalography

M.V. Petrenko, A.S. Pazgalev, and A.K. Vershovskii*
Ioffe Institute, St. Petersburg 194021, Russia

(Received 28 March 2023; revised 29 June 2023; accepted 12 July 2023; published 1 August 2023)

We present the concept and the results of an investigation of an all-optical vector-magnetic-field sensor scheme developed for biological applications such as nonzero-field magnetoencephalography and magnetocardiography. The scheme differs from the classical two-beam Bell-Bloom scheme in that the detecting laser beam is split into two beams, which are introduced into the cell in orthogonal directions, and the ratio of the amplitudes of the magnetic resonance signals in these beams and their phase difference are measured; strong optical pumping from the lower hyperfine level of the ground state ensures the resonance line narrowing, and detection in two beams is carried out in balanced schemes by measuring the beam-polarization rotation. The proposed sensor is compact, resistant to variations of parameters of laser radiation and highly sensitive to the angle of deflection of the magnetic field vector—with an estimated scalar sensitivity of the order of 16 $fT/Hz^{1/2}$ in the $8 \times 8 \times 8$ mm^3 cell, an angular sensitivity of 4×10^{-7} rad, or 0.08", was demonstrated.

DOI: 10.1103/PhysRevApplied.20.024001

I. INTRODUCTION

In recent decades, a rapid growth of interest in the problems of studying ultraweak magnetic fields generated by brain activity (magnetoencephalography, "MEG") has been observed. This is due to the advent of compact optical magnetic field (MF) sensors that can replace expensive superconducting quantum interference device (SQUID) systems [1] and overcome their inherent limitations. The principle of operation of these sensors is based on the effect of optically detected magnetic resonance (MR) in alkali atoms [2–7]; relaxation in the cells is suppressed by applying a special coating [8,9] or adding a buffer gas [10,11]. The first option makes it possible to achieve record relaxation times and, accordingly, narrow magnetic resonance lines, while the second option makes it possible to manufacture small-sized cells by simple means and heat them to relatively high ($> 70^{\circ}C$) temperatures. Therefore, sensors designed for use in MEG arrays typically use cells filled with a buffer gas.

The highest sensitivity to date is demonstrated by zero-MF optical sensors using the SERF effect [2,3,12–14]. However, the growing need for sensors capable of operating outside stationary magnetically isolated rooms has given impetus to research on the possibility of adapting nonzero MF sensors to MEG tasks [7,9,15]. These sensors are initially characterized by somewhat worse sensitivity, but their use can significantly reduce the requirements for the parameters of an external MF [7].

Nonzero MF alkaline sensors atoms are characterized by one more drawback: they measure the modulus of the magnetic field, but not its components. In MEG, this feature leads to the fact that, in the presence of a relatively strong external MF $\mathbf{B_0}$, they respond only to the component of the brain field, which is collinear to the $\mathbf{B_0}$ vector. Since the field generated by systems of magnetic shields and/or magnetic coils is spatially inhomogeneous, the task of interpreting the MEG signal in a nonzero MF requires knowing the direction of the vector $\mathbf{B_0}$ at the location of each sensor.

At the time of writing, there are a number of techniques that convert a scalar nonzero field sensor into a vector one, based both on measuring the response to a calibrated change in the transverse MF components [16–19], and on the observation of two or three components of the magnetic moment [20–22]. The latter technique was proposed in Ref. [23], and then in our earlier work [24] a modification that makes it possible to exclude the system of magnetic coils from the scheme was described. In this work, we have used the principles outlined in Refs. [23,24], modifying them for use in a compact all-optical compact sensor.

In this paper, we present a scheme of an all-optical nonzero field vector magnetometer-variometer based on a scalar nonzero field sensor built according to the Bell-Bloom scheme [15,25–27]. The scheme differs from the classical two-beam Bell-Bloom scheme primarily in that the detecting laser beam is split into two beams, which propagate through the cell in orthogonal directions. The ratio of the amplitudes of the MR signals in these beams and the difference in their phases are measured. The

*antver@mail.ioffe.ru

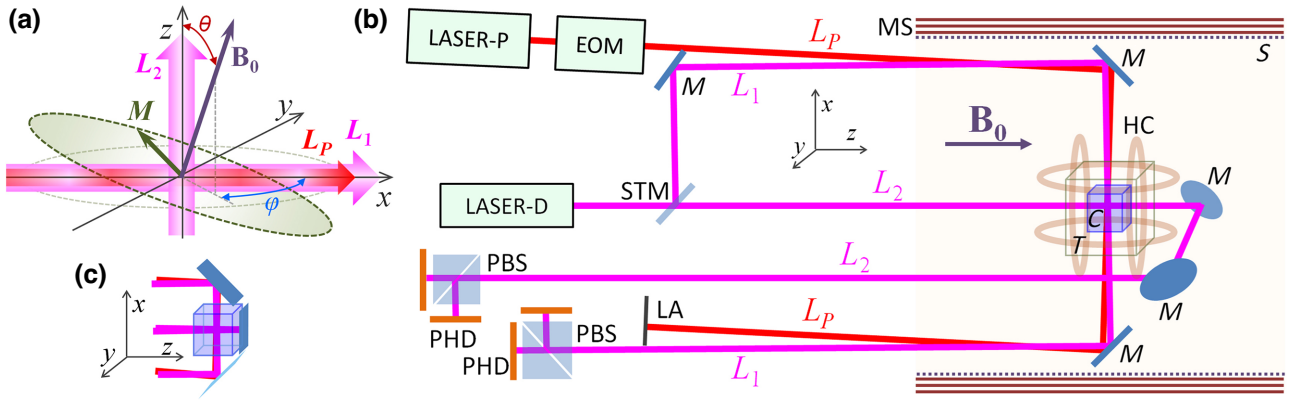

FIG. 1. (a) Pump and detection scheme: L_p is the pumping beam, L_1, L_2 are the detecting beams, $\mathbf{B_0}$ is the external magnetic field vector, **M** is the magnetic moment. (b) Simplified scheme of the experiment: the sensor includes the following: LASER-P, pumping light source; LASER-D, detecting light source; EOM, electro-optical modulator; *M*, mirror; STM, semitransparent mirror; *C*, gas cell with Cs vapor; *T*, thermostat; LA, light absorber; PBS, polarizing beam-splitter cube; PHD, balanced photodetectors. Elements of the experimental setup (not included in the sensor scheme) are as follows: MS, magnetic shield: *S*, solenoid; HC, two-coordinate Helmholtz coils system. (c) Possible modification of the scheme: a return mirror in the beam L_2.

proposed sensor is characterized by compactness (since an additional beam can be added to the scheme without increasing its size), high sensitivity to the MF vector deviation at the level of 0.1", and resistance to the laser radiation parameters' variations.

II. BASIC PRINCIPLES

The scheme under consideration uses a number of principles previously used by us in Ref. [27]. First, for pumping and excitation of the MR, it uses a beam with ellipticity modulated at a frequency $\omega \approx \omega_0$, where ω_0 is the Larmor precession frequency. Beam polarization changes from left to right circular. Secondly, we use combined hyperfine-Zeeman pumping, which was proposed in Ref. [28] and received a theoretical basis in Ref. [29]. The pump beam frequency is tuned to resonance with the D_1 transitions of the alkali metal line, which couple the hyperfine level $F = I - 1/2$ (where I is the nuclear spin) of $S_{1/2}$ state with the levels $F' = I \pm 1/2$ of $P_{1/2}$ state [28,29]. Zeeman pumping of $F = I + 1/2$, $m_F = F$ level is due to (i) partial overlapping of the optical absorption contours of two ground-state hyperfine transitions, and (ii) conservation of the nuclear component of the moment in the excited state [29]. Thirdly, we use strong optical pumping, which allows us to collect most of the atoms at the level $F = I + 1/2$, $m_F = F$. Happer called this state "end state" or "stretched" and showed [30] that the spin-exchange rate in this state can significantly decrease.

Let L_P denote the pumping beam [Fig. 1(a)]. It is directed along the x axis and modulated at the frequency ω. The magnetic field $\mathbf{B_0}$ is initially directed along the z axis. Pumping creates a magnetic moment **M** along beam L_P, whose component perpendicular to $\mathbf{B_0}$ precesses around $\mathbf{B_0}$. The pumping efficiency in the first approximation is proportional to the sine of the angle between L_P and $\mathbf{B_0}$. L_1, L_2 are the detecting beams, generated by the same laser. Their intensities are I_1 and I_2, respectively. The beams are linearly polarized and far detuned from the D_1 absorption line. Beam L_1 is directed along the x axis, beam L_2 is directed along the z axis.

The signals of the rotation of the polarization azimuth of the detecting beams L_1 and L_2 are detected at the frequency ω. The method of synchronous detection determines their amplitudes S_1, S_2 and phases ψ_1, ψ_2 with respect to the modulation signal. The amplitudes are proportional to the projections of the rotating component of **M** on the direction of their propagation (the so-called M_X scheme [31,32]). The S_1 signal, as in a conventional M_X magnetometer, is used to tune the frequency ω to the MR frequency ω_0. In addition, it is used as a reference signal in the processing of the S_2 signal, which makes it possible to determine the MF deflection angles regardless of the L_P, L_1, L_2 parameters.

Let us switch to a spherical coordinate system defined by the polar angle θ and the azimuthal angle ϕ [Fig. 1(a)]. It is easy to show that, within this simplified model, the angles θ and ϕ are expressed in terms of the phase difference ψ_1 and ψ_2 and the ratio S of the signals S_1 and S_2, normalized to the ratio of the intensities of the corresponding beams:

$$\phi = \psi_2 - \psi_1;$$
$$S \equiv \frac{|S_2|I_1}{|S_1|I_2} = k\frac{\sin\theta}{\sqrt{1-\sin^2(\theta)\cos^2(\phi)}}, \qquad (1)$$

where k is the scale factor that takes into account the inequality of the volumes of intersection of beams L_1 and L_2 with the pumping beam L_P.

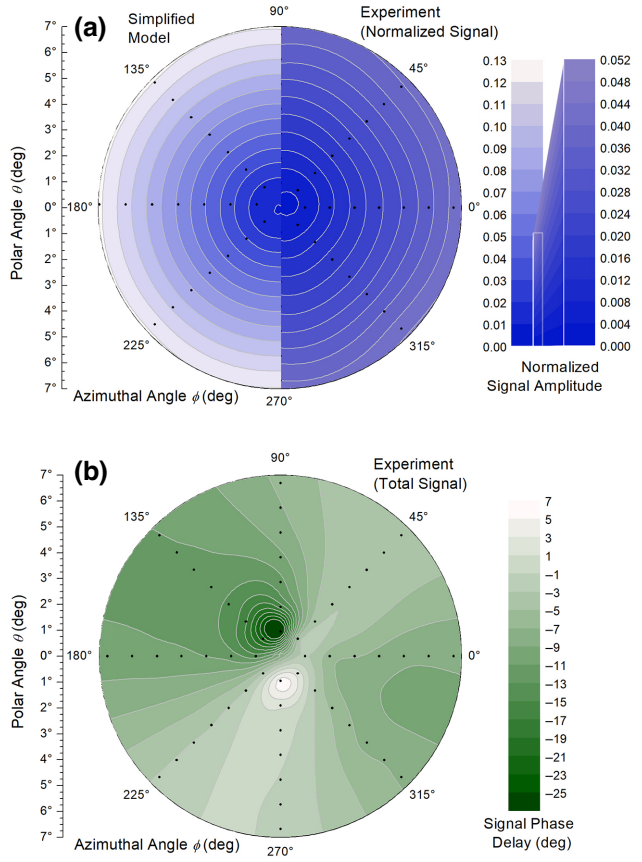

FIG. 2. (a) Amplitude S of the normalized vector signal: on the left, predictions of the simplified model [Eq. (1)], on the right, experiment. (b) Phase delay $\psi_2 - \psi_1 - \phi$ of the normalized vector signal. $\Gamma = 100$ nT, $B_0 = 3000$ nT.

For $\phi = 0°$ $S = \tan(\theta)$, for $\phi = 90°$ $S = \sin(\theta)$; at small θ $S \approx \theta$ for any ϕ.

Let us estimate the achievable sensitivities to variations in the transverse field components. In the ideal case ($\theta \approx 0$, $I_1 \approx I_2$), neglecting the second-order terms, we obtain

$$\delta B_x = \delta B_y \approx \frac{1}{k}\frac{\omega}{\Gamma}\delta B, \tag{2}$$

where Γ is the relaxation rate (MR half-width), and the scalar sensitivity $\delta B \approx \delta B_z$ is determined by the well-known expression

$$\delta B = \frac{\Gamma}{\gamma}\frac{n}{S_1}, \tag{3}$$

where γ is the gyromagnetic ratio and n is the spectral density of the principal quantum noise (atomic projection noise plus photon shot noise; in optimized schemes, these two noises are approximately equal in spectral power). The transverse sensitivity $\delta B_\perp = \delta B_x = \delta B_y$ turns out to be $(1/k)(\omega/\Gamma)$ times worse than δB.

Let us estimate the angular sensitivity for small θ:

$$\delta\theta = \frac{1}{k}\left(\frac{S_1}{n}\right)^{-1}, \tag{4}$$

$$\delta\phi = \left(\frac{S_2}{n}\right)^{-1} \approx \frac{\delta\theta}{\theta}. \tag{5}$$

As expected, the polar angle sensitivity is independent of B_0, and is determined by the signal-to-noise ratio in the L_1 beam. Uncertainty $\delta\phi$ at large θ approaches $\delta\theta$, but at small θ tends to infinity; this is due not to the features of the proposed scheme, but to the general properties of the spherical coordinate system.

III. EXPERIMENTAL SETUP

Measurements were made on the setup [27,33], modified in accordance with the task of the experiment [Fig. 1(b)]. The light sources were diode lasers with an external cavity manufactured by VitaWawe. The pumping laser frequency was tuned to the Cs D_1 transitions, which couple the hyperfine level $F = 3$ of the $S_{1/2}$ state to the levels $F' = 3$, $F' = 4$ of the $P_{1/2}$ state. The frequency of the detecting laser was tuned 15–20 GHz down from the D_1-line transitions linking the level $F = 4$ of the $S_{1/2}$ state with the levels $F' = 3$, $F' = 4$ of the $P_{1/2}$ state.

A Thorlabs electro-optical modulator was used to modulate the pumping light polarization. The available pumping light power at the cell input was 5.4 mW, the detecting light power ($L_1 + L_2$) was set at 4.9 mW. The sensitive element of the sensor was a cubic cell $8 \times 8 \times 8$ mm^3 containing saturated cesium vapor and nitrogen at a pressure of approximately 100 Torr. A thermostat with a cell and a heater were placed in the central region of a multilayer magnetic shield, in which the MF induction varied within 0.1–12 μT.

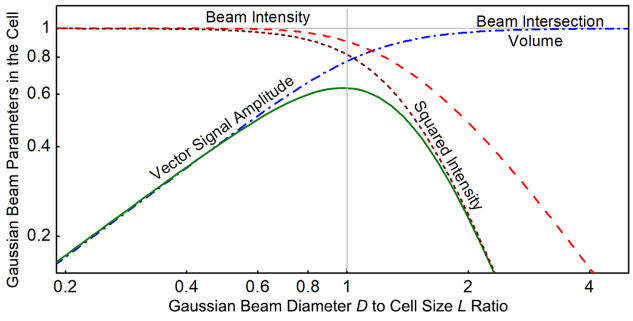

FIG. 3. Calculated dependence of the magnitude of the vector signal and the intensity of the Gaussian beam of diameter D in a cubic cell with face length L.

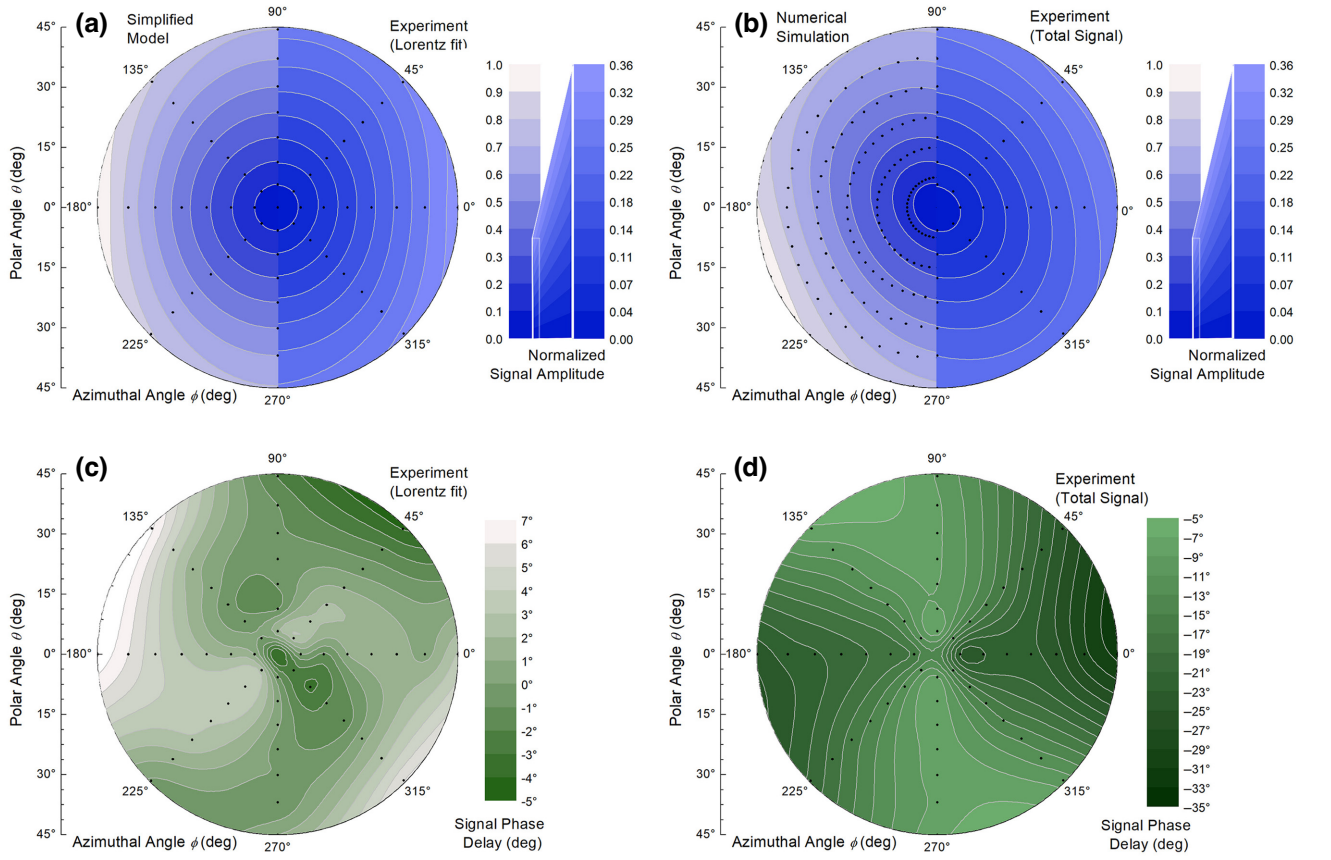

FIG. 4. (a) Amplitude S_L of the Lorentzian part of the normalized vector signal: on the left, the predictions of the simplified model [Eq. (1)], on the right, the experiment. (b) Amplitude S_T of the total normalized vector signal: on the left, the result of numerical simulation, on the right, the experiment. (c) Phase delay $\psi_{2L} - \psi_{1L} - \phi$ of the part of the Lorentzian part of the normalized vector signal. (d) Phase delay $\psi_{2T} - \psi_{1T} - \phi$ of the total normalized vector signal. $\Gamma = 100$ nT, $B_0 = 500$ nT.

The cell temperature was maintained at 93°C, which ensured the maximum scalar sensitivity achievable for the given experimental parameters [34].

We used a configuration with all three beams passing through the cell once, which required the installation of two mirrors behind the cell at an angle of 45° to beam L_2 [Fig. 1(b)], and resulted in an increase in the volume of the sensor. However, the compactness of the sensor can be preserved (and, at the same time, its vector sensitivity can be increased) by installing a mirror [Fig. 1(c)] in the thermostat that returns the L_2 beam back through the entrance window at a small angle (as was done, for example, in Ref. [35]). In this case, the length of interaction of the beam L_2 with the optically oriented media will double. This will lead to a proportional increase in the signal S_2 (and a corresponding change in k), but, possibly, will require an increase in the detuning of the detecting laser from the optical transition. The same technique can be applied to the beams L_P and L_1.

The noise spectrum of the vector sensor was studied by applying a calibrated transverse field with an amplitude of 100 pT (rms), oscillating at 10 Hz.

IV. RESULTS

A typical distribution of the parameters of the vector signal S at small polar angles θ and MFs, significantly exceeding the half-width Γ of the MR, is shown in Fig. 2. It can be seen that the signal amplitude is fairly well described by Eq. (1), and the value of k is $k = 0.40 \pm 0.01$; in accordance with Eq. (5), the measurement uncertainty $\delta\phi$ increases with decreasing θ.

By numerical integration, we calculated the overlap integral of the beams L_P and L_2 under the assumption that they are characterized by the same diameter D (Fig. 3), and approximated the resulting dependence by the expression

$$k = \frac{r/1.16}{(1 + (r/1.16)^4)^{\frac{1}{4}}}, \tag{6}$$

where $r = D/L$ is the ratio of the diameter of the beams to the length of the edge of the cubic cell L. An increase in D leads to an increase in the vector sensitivity, but also to light losses: for each beam, the dependence of the intensity of the light entering the cell on r is described by the

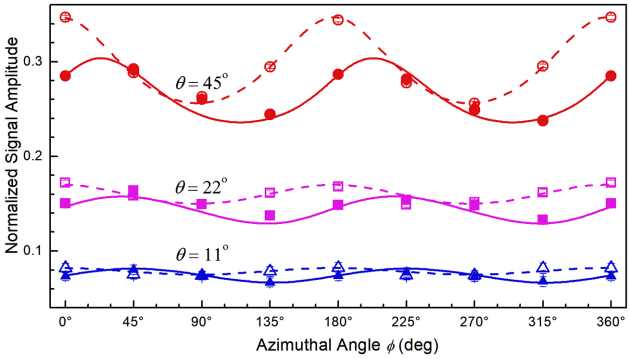

FIG. 5. Dependence of the vector signals S_L and S_T at $\Gamma = 100$ nT, $B_0 = 500$ nT, $\theta = 11°, 22°, 45°$ on the azimuthal angle ϕ: dashed lines, predictions of the simplified model [Eq. (1)], open symbols, experiment (the amplitude S_L of the Lorentzian contour); solid lines are the result of numerical simulation, filled symbols are the experiment (the amplitude S_T of the total signal).

approximate formula

$$I = (1 + (r/1.4)^4)^{-0.44}, \tag{7}$$

the signal being proportional to the product of the intensities of the pump and detection beams. The final dependence of the magnitude of the vector signal on r has a maximum at $r \approx 1$. These estimates do not take into account changes in the scalar sensitivity, which, other

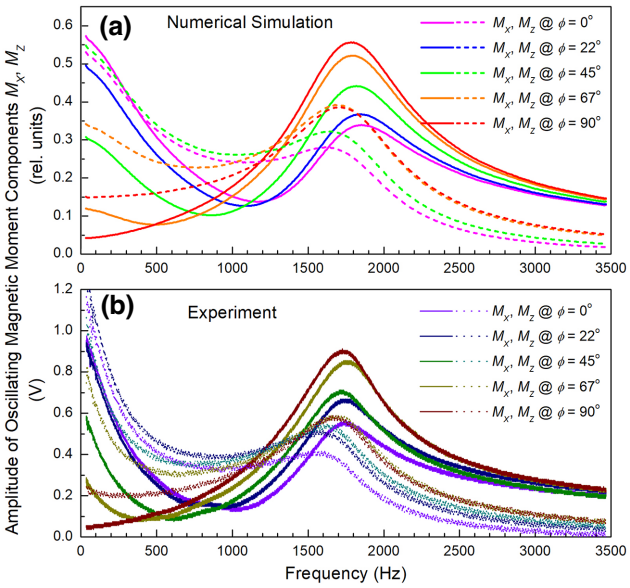

FIG. 6. Dependence of the x and z components of the magnetic moment **M** on the pump-beam modulation frequency: (a) the result of numerical simulation, (b) the experiment (the measured values of M_Z are multiplied by $1/k = 2.5$ to take into account the difference in the sensitivities of the Z and X channels). $\Gamma = 100$ nT, $B_0 = 500$ nT, $\theta = 45°$.

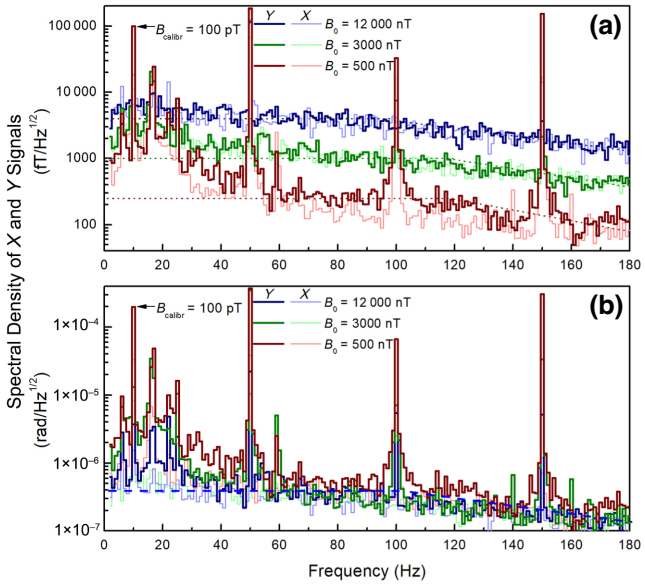

FIG. 7. Spectral dependence of vector signal noise (X and Y channels) at three values of the field B_0: (a) in magnetic field units, (b) in angular units. A calibrated magnetic field disturbance $B_Y = 100$ pT rms is applied to coil Y. 50-Hz signals and their harmonics are mains' interference.

parameters being constant, is proportional to the root of the number of interrogated atoms [36] and depends in a complex way on the pump intensity [27].

In our experiment, $r = 0.575$, and $k = 0.40 \pm 0.01$, which is quite close to the value of $k(r) = 0.49$ predicted by Eq. (6). The remaining difference can be explained by the depolarizing properties of the mirrors located on the path of the beam after the cell: the phase delay introduced by the mirrors leads to a partial transformation of the rotation of the polarization azimuth into its ellipticity.

The difference between the experiment and the predictions of the simplified theory is manifested at relatively small fields and large deflection angles θ (Fig. 4, $B_0 \approx 5\,\Gamma/\gamma$).

The signals measured in our experiment when scanning the frequency ω in the vicinity of ω_0 were approximated by Lorentzian contours with quadratic baselines. The amplitudes S_{2L}, S_{1L} (and their ratio S_L) of the contours and phases ψ_{2L}, ψ_{1L} were calculated. The amplitudes S_{2T}, S_{1T} (and their ratio S_T) and the phases ψ_{2T}, ψ_{1T} of the total signals (i.e., the signals that are measured in a real sensor) were also calculated.

The simplified model [Eq. (1)] describes well the parameters of the Lorentzian contour [Fig. 4(a)], but does not provide a correct description of the total signal S_T. To do this, we carried out a numerical simulation: the dynamics of the magnetic moment was described by a system of nonstationary Bloch equations under conditions of periodic pumping. As can be seen from Figs. 4(b) and 5(b), the

TABLE I. The results of the study of the parameters of the vector sensor.

No.	Parameter	Designation	Expected value	Experiment	Units
1	Cubic-cell face length	L	–	8.0 ± 0.2	mm
2	Pump-detection beam diameter	D	–	4.6 ± 0.3	mm
3	The power of the beams L_1, L_2 on the photodetectors	I_1, I_2	–	0.70 ± 0.05	mW
4	Amplitude of the signal in L_1 at B_0 = 500 nT, $\theta = 0$	S_1	–	0.19 ± 0.01	mA
5	Magnetic resonance half-width	Γ	–	$2\pi \times (350 \pm 6)$	Hz
6	Shot-noise spectral density	n_{sh}	12.6	–	pA/Hz$^{1/2}$
7	Signal-to-noise ratio in L_1 (shot noise)	S_1/n_{sh}	1.5×10^7	–	
8	Ultimate sensitivity (shot noise)	δB_{sh}	6	–	fT/Hz$^{1/2}$
9	Total noise spectral density	n	$3 \times n_{sh}$	–	–
10	Ultimate sensitivity (total noise)	δB	18	16 ± 3[a]	fT/Hz$^{1/2}$
11	Signal-to-noise ratio in L_1 (total noise)	S_1/n	5×10^6	$6.2 \pm 1.3 \times 10^6$ [a]	
12	Scale factor	k	0.49	0.40 ± 0.01	–
13	Angular resolution	$\delta\theta$	0.41	0.39 ± 0.08[b]	μrad
14	Sensitivity to field components at $B_0 = 500$ nT	$\delta B_\perp$	230	220 ± 50[b]	fT/Hz$^{1/2}$
15	MF transverse noise spectral density	n_{MF}	–	130 ± 50[b]	fT/Hz$^{1/2}$
16	Angular resolution (corrected)	$\delta\theta$'	0.41	0.35 ± 0.08[c]	μrad
17	Sensitivity to field components at $B_0 = 500$ nT (corr.)	$\delta B_\perp$'	230	180 ± 80[c]	fT/Hz$^{1/2}$

[a]Derived from the value given in line 13 using Eqs. (3), (4).
[b]Derived from the experimental data (Fig. 7) taken in the frequency range of 65–90 Hz
[c]Derived from the values (lines 13–14): the contribution of the MF transverse noise (line 15) is excluded.

numerical simulation adequately describes the total signal S_T.

The calculated and experimental spectra of the magnetic resonance signal in a weak field are shown in Fig. 6. As it turned out, the distortion of the shape of the resonance is due to another signal, which is maximum at zero modulation frequency. It arises when the vector $\mathbf{B_0}$ deviates in the 0-x-y plane, and is due to the nonprecessing component of the magnetic moment, oriented along $\mathbf{B_0}$ and changing its sign twice during the modulation period. The wing of this signal is added to the Lorentzian contour of the M_X resonance, which leads to its distortion and phase shift.

Figure 7 shows the results of measurements of the transverse noise spectral density in a magnetic shield.

V. DISCUSSION

From the above results, it follows that the complex nature of the spectrum of the signals S_{1T} and S_{2T} does not lead to a deterioration in the parameters of the vector sensor, but requires corrections for the calculation of θ and ϕ.

Vector angular sensitivity is measured at the level of (0.39 ± 0.1) μrad (see Fig. 7), or 0.08". As follows from Eqs. (2), (4), (5), the sensitivity to the transverse field components $\delta B_\perp$ deteriorates with increasing B_0, while the angular sensitivity does not depend on B_0.

The results of the study of the parameters of the vector sensor are shown in Table I. The estimated values given in Table I are calculated using Eqs. (2)–(6) and the values in lines 1–5 of Table I; it is also taken into account that, according to Refs. [27,33], the magnitude of real noise (including atomic projection noise and technical noise of laser radiation) under our experimental conditions is approximately 3 times higher than the shot-noise level.

Comparing the data in Table I with the results obtained by other groups is not a straightforward task, since different researchers take measurements with different time resolutions and report results in different units. Below we attempt to offer examples that give an idea of the vector sensitivity achievable with an atomic magnetometer.

In Ref. [20], an angular resolution of 10 μrad for integration times from 10 s up to 2000 s is declared. In Ref. [22] with a measurement time of 100 ms, sensitivity of 0.34 mrad was achieved, while Refs. [19] and [21] report sensitivity of 0.5 and 1.7 mrad/Hz$^{1/2}$, respectively. [37] reports on an overall angular resolution of 0.63 mrad. The following papers give an estimate of the sensitivity to the magnetic field components: [38,39] – 1 pT/Hz$^{1/2}$, [40] – 54 fT/Hz$^{1/2}$. However, it should be noted that sensors described in Refs. [19–21,37,40] use big paraffin-coated or filled with helium cells; radiofrequency coils are used in Refs. [20,37,39]; MF coils are used in Refs. [20,38–40], and more than two lasers are used in Refs. [20,21,40]. The properties listed above may prevent the use of these schemes in MEG.

Since the typical value of the noise of the longitudinal field component in the frequency range free from acoustic disturbances in our shield is approximately equal to 0.6 pT/Hz$^{1/2}$ [41] (which is about 5 times the noise of the transverse field components), a direct measurement of the real signal-to-noise ratio and the real scalar sensitivity

of our sensor is possible only in the gradiometric scheme [34,41]. However, the use of the vector scheme provides us with an indirect tool for measuring these quantities. From the results of measuring the angular resolution $\delta\theta$ in a strong enough MF, using Eq. (4), one can determine the real signal-to-noise ratio S_1/n, and then, using Eq. (3), the real scalar sensitivity δB. The estimated values given in Table I (lines 10–14) are in excellent agreement with the experimental results.

According to Eqs. (2)–(5), the achieved sensitivity to the field components can be improved more than twofold by doubling the beam diameters in the cell with a corresponding fourfold increase in the integrated power. It should also be taken into account that in this case, the scalar sensitivity will double [36] (proportionally to the root of the number of interrogated atoms), and the overall improvement will be almost fivefold.

This expected vector sensitivity approaches that required of the three-component sensor for operation in MEG complexes; this is indirectly confirmed by the results of Ref. [42]. In any case, the achieved angular sensitivity is certainly sufficient to measure the direction of the external MF vector in nonzero-field MEG systems. Sensitivity $\delta B_\perp$ can be further improved by reducing the field to $B_0 \approx \Gamma/\gamma$; in our experiment, this is prevented by low-frequency noise and modulations of laser radiation. In this case, the transverse sensitivity can reach its limit value of $\delta B_\perp \approx \delta B$.

VI. CONCLUSIONS

We have demonstrated the operability of the proposed concept, and have shown that the parameters of the scheme correspond to the calculated ones. Due to the use of a reference detecting beam, the measurement result of the magnetic field deflection angles is not affected by variations in the spectral parameters of the pumping and detecting beams. The proposed scheme can be implemented in the same sensor dimensions as the Bell-Bloom scheme or the standard two-beam M_X magnetometer scheme. The demonstrated parameters allow real-time measurement of the distribution of external MF vector directions in nonzero-field MEG complexes. A further (almost fivefold) improvement in angular sensitivity can be achieved by increasing the beam diameters with a corresponding increase in the pump and detection powers. This will require the use of high-power, low-noise pump, and detection laser sources; but in this case, the sensitivity of the proposed sensor will be sufficient to measure all three components of the MEG vector signal in a nonzero magnetic field. An additional, but useful in laboratory conditions, result of this work is an alternative method for determining the scalar sensitivity of the sensor under conditions when the MF noise significantly exceeds the level of intrinsic noise.

[1] D. Cohen, Magnetoencephalography: Detection of the brain's electrical activity with a superconducting magnetometer, Science **175**, 664 (1972).

[2] I. K. Kominis, T. W. Kornack, J. C. Allred, and M. V. Romalis, A subfemtotesla multichannel atomic magnetometer, Nature **422**, 596 (2003).

[3] J. Iivanainen, M. Stenroos, L. Parkkonen, and Measuring meg closer to the brain, Performance of on-scalp sensor arrays, NeuroImage **147**, 542 (2017).

[4] E. Boto, S. S. Meyer, V. Shah, O. Alem, S. Knappe, P. Kruger, T. M. Fromhold, M. Lim, P. M. Glover, P. G. Morris, R. Bowtell, G. R. Barnes, and M. J. Brookes, A new generation of magnetoencephalography: Room temperature measurements using optically-pumped magnetometers, NeuroImage **149**, 404 (2017).

[5] K.-M. C. Fu, G. Z. Iwata, A. Wickenbrock, and D. Budker, Sensitive magnetometry in challenging environments, AVS Quantum Sci. **2**, 044702 (2020).

[6] N. V. Nardelli, A. R. Perry, S. P. Krzyzewski, and S. A. Knappe, A conformal array of microfabricated optically-pumped first-order gradiometers for magnetoencephalography, EPJ Quantum Technol. **7**, 11 (2020).

[7] M. Limes, E. Foley, T. Kornack, S. Caliga, S. McBride, A. Braun, W. Lee, V. Lucivero, and M. Romalis, Portable Magnetometry for Detection of Biomagnetism in Ambient Environments, Phys. Rev. Appl. **14**, 011002 (2020).

[8] H. Wang, T. Wu, W. Xiao, H. Wang, X. Peng, and H. Guo, Dual-Mode Dead-Zone-Free Double-Resonance Alignment-Based Magnetometer, Phys. Rev. Appl. **15**, 024033 (2021).

[9] R. Zhang, W. Xiao, Y. Ding, Y. Feng, X. Peng, L. Shen, C. Sun, T. Wu, Y. Wu, Y. Yang, Z. Zheng, X. Zhang, J. Chen, and H. Guo, Recording brain activities in unshielded earth's field with optically pumped atomic magnetometers, Sci. Adv. **6**, eaba8792 (2020).

[10] V. Lucivero, W. Lee, N. Dural, and M. Romalis, Femtotesla Direct Magnetic Gradiometer using a Single Multipass Cell, Phys. Rev. Appl. **15**, 014004 (2021).

[11] A. R. Perry, M. D. Bulatowicz, M. Larsen, T. G. Walker, and R. Wyllie, All-optical intrinsic atomic gradiometer with sub-20 ft/cm/$\sqrt{Hz}$ sensitivity in a 22 μt earth-scale magnetic field, Opt. Express **28**, 36696 (2020).

[12] M. J. Brookes, J. Leggett, M. Rea, R. M. Hill, N. Holmes, E. Boto, and R. Bowtell, Magnetoencephalography with optically pumped magnetometers (opm-meg): The next generation of functional neuroimaging, Trends Neurosci. **45**, 621 (2022).

[13] J. Iivanainen, R. Zetter, and L. Parkkonen, Potential of on-scalp MEG: Robust detection of human visual gamma-band responses, Hum. Brain Mapp. **41**, 150 (2020).

[14] M. Rea, E. Boto, N. Holmes, R. Hill, J. Osborne, N. Rhodes, J. Leggett, L. Rier, R. Bowtell, and V. Shah *et al.*, A 90-channel triaxial magnetoencephalography system using optically pumped magnetometers, Ann. N. Y. Acad. Sci. **1517**, 107 (2022).

[15] Y. Guo, S. Wan, X. Sun, and J. Qin, Compact, high-sensitivity atomic magnetometer utilizing the light-narrowing effect and in-phase excitation, Appl. Opt. **58**, 734 (2019).

[16] O. Gravrand, A. Khokhlov, J. Le Mouël, and J. Léger, On the calibration of a vectorial ^{4}He pumped magnetometer, Earth, Planets Space **53**, 949 (2001).

[17] R. E. Slocum and L. J. Ryan, in *NASA Earth Science Technology Conference (ESTC) June 24–26 2003, the University of Maryland Inn and Conference Center* (2003).

[18] A. K. Vershovskiĭ *et al.*, A new method of absolute measurement of the three components of the magnetic field, Opt. Spectrosc. **101**, 309 (2006).

[19] B. Patton, E. Zhivun, D. Hovde, and D. Budker, All-Optical Vector Atomic Magnetometer, Phys. Rev. Lett. **113**, 013001 (2014).

[20] S. Afach, G. Ban, G. Bison, K. Bodek, Z. Chowdhuri, Z. Grujić, L. Hayen, V. Hélaine, M. Kasprzak, and K. Kirch *et al.*, Highly stable atomic vector magnetometer based on free spin precession, Opt. Express **23**, 22108 (2015).

[21] W.-M. Sun, Q. Huang, Z.-J. Huang, P.-W. Wang, and J.-H. Zhang, All-optical vector cesium magnetometer, Chin. Phys. Lett. **34**, 058501 (2017).

[22] R. Zhang, R. Mhaskar, K. Smith, E. Balasubramaniam, and M. Prouty, Vector measurements using all optical scalar atomic magnetometers, J. Appl. Phys. **129**, 044502 (2021).

[23] A. Fairweather and M. Usher, A vector rubidium magnetometer, J. Phys. E: Sci. Instrum. **5**, 986 (1972).

[24] A. K. Vershovskii, Project of laser-pumped quantum M_X magnetometer, Tech. Phys. Lett. **37**, 140 (2011).

[25] I. Fescenko, P. Knowles, A. Weis, and E. Breschi, A Bell-Bloom experiment with polarization-modulated light of arbitrary duty cycle, Opt. Express **21**, 15121 (2013).

[26] Z. D. Grujić and A. Weis, Atomic magnetic resonance induced by amplitude-, frequency-, or polarization-modulated light, Phys. Rev. A **88**, 012508 (2013).

[27] M. V. Petrenko, A. S. Pazgalev, and A. K. Vershovskii, Single-Beam All-Optical Non-Zero Field Magnetometric Sensor for Magnetoencephalography Applications, Phys. Rev. Appl. **15**, 064072 (2021).

[28] T. Scholtes, V. Schultze, R. IJsselsteijn, S. Woetzel, and H.-G. Meyer, Light-narrowed optically pumped m_x magnetometer with a miniaturized cs cell, Phys. Rev. A **84**, 043416 (2011).

[29] E. N. Popov, V. A. Bobrikova, S. P. Voskoboinikov, K. A. Barantsev, S. M. Ustinov, A. N. Litvinov, A. K. Vershovskii, S. P. Dmitriev, V. A. Kartoshkin, A. S. Pazgalev, and M. V. Petrenko, Features of the formation of the spin polarization of an alkali metal at the resolution of hyperfine sublevels in the $^2s_{1/2}$ state, JETP Lett. **108**, 513 (2018).

[30] S. Appelt, A. Ben-Amar Baranga, A. R. Young, and W. Happer, Light narrowing of rubidium magnetic-resonance lines in high-pressure optical-pumping cells, Phys. Rev. A **59**, 2078 (1999).

[31] A. L. Bloom, Principles of operation of the rubidium vapor magnetometer, Appl. Opt. **1**, 61 (1962).

[32] V. Schultze, B. Schillig, R. IJsselsteijn, T. Scholtes, S. Woetzel, and R. Stolz, An optically pumped magnetometer working in the light-shift dispersed Mz mode, Sensors **17**, 561 (2017).

[33] A. K. Vershovskii and M. V. Petrenko, Methods of parametric resonance excitation in the scheme of an optical magnetometric sensor, Tech. Phys. **66**, 821 (2021).

[34] M. V. Petrenko, S. P. Dmitriev, A. S. Pazgalev, A. E. Ossadtchi, and A. K. Vershovskii, Towards the non-zero field cesium magnetic sensor array for magnetoencephalography, IEEE Sens. J. **21**, 18626 (2021).

[35] A. Borna, T. R. Carter, J. D. Goldberg, A. P. Colombo, Y.-Y. Jau, C. Berry, J. McKay, J. Stephen, M. Weisend, and P. D. D. Schwindt, A 20-channel magnetoencephalography system based on optically pumped magnetometers, Phys. Med. Biol. **62**, 8909 (2017).

[36] D. Budker and M. Romalis, Optical magnetometry, Nat. Phys. **3**, 227 (2007).

[37] S. J. Ingleby, C. O'Dwyer, P. F. Griffin, A. S. Arnold, and E. Riis, Vector Magnetometry Exploiting Phase-Geometry Effects in a Double-Resonance Alignment Magnetometer, Phys. Rev. Appl. **10**, 034035 (2018).

[38] S. Seltzer and M. Romalis, Unshielded three-axis vector operation of a spin-exchange-relaxation-free atomic magnetometer, Appl. Phys. Lett. **85**, 4804 (2004).

[39] W. Zheng, S. Su, G. Zhang, X. Bi, and Q. Lin, Vector magnetocardiography measurement with a compact elliptically polarized laser-pumped magnetometer, Biomed. Opt. Express **11**, 649 (2020).

[40] G. Bison, V. Bondar, P. Schmidt-Wellenburg, A. Schnabel, and J. Voigt, Sensitive and stable vector magnetometer for operation in zero and finite fields, Opt. Express **26**, 17350 (2018).

[41] M. Petrenko and A. Vershovskii, Towards a practical implementation of a single-beam all-optical non-zero-field magnetic sensor for magnetoencephalographic complexes, Sensors **22**, 9862 (2022).

[42] R. J. Clancy, V. Gerginov, O. Alem, S. Becker, and S. Knappe, A study of scalar optically-pumped magnetometers for use in magnetoencephalography without shielding, Phys. Med. Biol. **66**, 175030 (2021).